Proceedings Paper:

DYNAMICS OF FULLY RESOLVED BINARY PARTICLE INTERACTIONS IN ISOTROPIC TURBULENCE

L. F. Mortimer, M. Fairweather, D. O. Njobuenwu

School of Chemical & Processing Engineering
University of Leeds, Leeds, LS2 9JT, United Kingdom

pmlfm@leeds.ac.uk

Abstract

Binary particle-particle interaction events in turbulence are simulated using the spectral element-based DNS solver, Nek5000 and an immersed boundaries method. Particle-fluid coupling is achieved using the ghost-cell approach. Two periodic boxes of isotropic turbulence are obtained via linear forcing with Taylor microscale Reynolds numbers, $Re_\lambda = 29$ and $Re_\lambda = 197$. These have been selected to match those typical in the bulk and viscous sublayer regions of a $Re_\tau = 180$ turbulent channel flow respectively. Both solid and fluid phase material and chemical properties are chosen to represent $100\mu m$ calcite particles in a $0.02m$ half-height channel flow. Simulations are initialised based on the most frequently occurring particle-particle collision events sampled from a four-way coupled DNS-LPT simulation. Particle interaction is modelled using interparticle forces based on DLVO theory and the hard sphere collision model.

Results indicate that particles in regions of increased turbulence are less likely to agglomerate, since their motion is dominated by the viscous and pressure forces on the particle, whereas in the bulk of the channel, forces transverse to streamwise motion allow pairs of particles travelling together to undergo agglomeration. Further variables of motion are monitored, such as angular velocity, in order to elucidate the effect of turbulence on a sphere's rotational behaviour. It is to be determined in future work how the chemical and material properties of both phases affect these trajectories and potential for agglomeration.

1   Introduction

Particle-laden turbulent flows occur commonly in both natural and industrial environments. Prediction of tidal currents, lung airways and liquid-fueled combustion are just a few cases where understanding of the particulate phase dynamics is of interest. The present work is of significance to the nuclear industry, where the formation and build-up of CRUD (Chalk-River unidentified deposit) on reactor fuel-pins stands as a performance and safety issue (Short et al., 2013).

The potential to elucidate the dynamics of particle-particle collisions and subsequent agglomerations would be invaluable in understanding the formation and characteristics of the depositing particulate structures.

With recent advances in computational power, providing capabilities to obtain greater levels of accuracy with high fidelity techniques, understanding multiphase systems has become of great interest in the recent literature. The combination of direct numerical simulation (DNS) of the continuous phase with Lagrangian particle tracking (LPT) of the discrete phase is frequently used to simulate such systems. In this approach, despite all relevant length-scales being resolved in the Eulerian phase, particles are modelled as point-like; therefore, information surrounding the small scale fluid-structure interaction is lost. Instead, models based on both empirical observation and higher fidelity simulations are used to provide, for example, such quantities as drag and lift coefficients. These estimate the influence of the local fluid field on the particle. This approach is highly effective in studying large ensembles of particles, where mean quantities can be studied to understand macroscopic behaviour. However, to fully determine the dynamics of small-scale motion and interaction (which are fundamental to and underpin the large scales), the flow field surrounding the particle must be fully resolved. Various methods of performing this have been developed in recent years (Mark & van Wachem, 2008; Tseng & Ferziger, 2003; Peskin, 2002; Hu, 1996), all of which offer a trade-off between accuracy and computational cost / complexity.

The work presented here uses an immersed boundary method (IBM), coupled to a spectral element method (SEM) based DNS solver to resolve the flow around dynamic particle meshes. The aim is to study the effect of turbulence on particle-particle interactions as turbulence intensities based on those present at varying wall-normal distances in a $Re_\tau = 180$ turbulent channel flow. By analysing the resulting trajectories and dynamic properties of the two-particle system, one can begin to develop an understanding of how (and under what conditions) particle

collisions or agglomerations occur, at levels of detail which greatly surpass those of LPT-based studies.

2 Mathematical formulation

The nature of the study requires that the smallest scales associated with turbulent flow structures are captured. Furthermore, with increasing grid nodal density, the particle mesh used in the immersed boundary solver obtains higher resolution with regards to flow-field feedback. The use of direct numerical simulation allows for both requirements to be met. The governing equations for the continuous phase are the Navier-Stokes (NS) equations, given as

$$\nabla \cdot \boldsymbol{u}_F = 0, \tag{1}$$

$$\frac{D\boldsymbol{u}}{Dt} = -\frac{1}{\rho_F}\nabla p + \nu_F\nabla^2\boldsymbol{u}_F + \boldsymbol{f}_{LF}, \tag{2}$$

where $\boldsymbol{u}_F$ is the fluid velocity vector, p is the fluid pressure, ρ_F is the density of the continuous phase, ν_F is the fluid kinematic viscosity and t represents time. The term $\boldsymbol{f}_{LF}$ is a linear force per unit mass, defined later. The Eulerian field equations are solved using the SEM based DNS solver, Nek5000 (Fischer et al., 2008) which employs a high order spectral element method and has been chosen due to its efficient parallel processing scaling capabilities. The code has also been tested extensively and possesses a strong validation history. During the transition to steady-state turbulence, a maximum courant number of 0.3 is used when adjusting the timestep.

The computational mesh consists of a box with length 2π in each direction, discretized into $48 \times 48 \times 48$ equally distributed cubic spectral elements of order $N = 7$. Periodic boundary conditions are enforced at $\pm\pi$ in each direction. The linear forcing method (Rosales & Meneveau, 2005; Lundgren, 2003) is used to drive the system to isotropic homogenous turbulence at two different Reynolds numbers (based on the Taylor microscale, λ). These are $Re_\lambda = 29$ and 197, where $Re_\lambda = \langle u_{rms}'\rangle\lambda/\nu_F$. Here, $\langle u_{rms}'\rangle$ is the averaged root mean square velocity fluctuation and ν_F is the kinematic viscosity of the fluid. In a turbulent channel flow, these Reynolds numbers are typical of the bulk flow and viscous sublayer regions respectively. The linear force per unit mass term is given by $\boldsymbol{f}_{LF} = A\boldsymbol{u}_F$ where A is a specified parameter relating to a specific turnover time scale. Tuning of this parameter allows one to obtain a desired turbulence level. The fluid-phase parameters are presented in Table I.

Re_λ	29	197
N_E	48^3	48^3
A	0.0667	0.1667
ρ_F	1	1
ν_F	4.491×10^{-3}	4.491×10^{-4}

TABLE I. DNS parameters for periodic cubes of linearly forced isotropic turbulence.

The particle is represented by a secondary computational mesh consisting of 320 faces, stored in the face-vertex representation. Each has associated a centroid position and velocity (based upon the global particle angular velocity). The immersed boundary (IB) condition is a Dirichlet boundary condition such that $\boldsymbol{u}_F = \boldsymbol{u}_P + \boldsymbol{\omega}_P \times \boldsymbol{r}_F$ on each particle face, F. Here, $\boldsymbol{u}_P$ is the particle linear velocity, $\boldsymbol{\omega}_P$ is the particle angular velocity and $\boldsymbol{r}_F$ is the position vector from the centre of the particle to the centroid of face F.

A second-order accurate ghost cell method is used to ensure the IB condition is met. Every timestep, each cell in the domain (formed by the bisectors between two neighbouring Gauss-Lobatto-Legendre points) is identified as a) external fluid, b) internal ghost-cell or c) internal fictitious fluid. A ghost cell is defined such that the IB intersects the cell and contains the cell mid-point. Internal and external fluid cells are those either inside or outside the IB, respectively. The velocities at the ghost-cells are maintained each timestep such that, through trilinear interpolation, the fluid velocity on the boundary is exactly the local face velocity.

To advect the particle, the surface forces (pressure and viscous) are calculated using the following equation:

$$F_j = \sum_{f=1}^{N_f}\left(-P^f\delta_{ij} + \tau_{ij}^f\right)n_j^f dS^f, \tag{3}$$

where F_j is the total translational force on the particle, f refers to the current face in the summation, with N_f being the total number of faces in the particle mesh, P^f is the pressure interpolated at the centroid of face f, τ_{ij} is the viscous stress tensor, n_j^f is a unit vector normal to the face f, and dS^f is the surface area of face f. A similar equation is used to calculate the viscous contributions to torque in the off-normal directions, used to update the angular velocity of the particle. The orientation of the mesh is tracked in a quaternion formulation. For further information on the particle rotation and angular velocity solver see Njobuenwu & Fairweather (2015).

Parameter	Value
r_P	$50\ \mu m$
e	0.4
ρ_P/ρ_F	2.71
A	22.3 zJ
n	$1 \times 10^{-3}\ M$
Θ	$20\ mV$
κ	$0.1\ nm^{-1}$
T_F	$300\ K$

TABLE II. IBA parameters for periodic cubes of linearly forced isotropic turbulence.

Particle collisions are performed using the inelastic hard-sphere approach, using a constant coefficient of restitution. In addition, a sphere-sphere DLVO (Derjaguin and Landau, 1941; Verwey and Overbeek, 1955) potential is used to calculate the van der Waals attraction and electric double layer repulsion between particle-pairs. The equation for the attraction or repulsion between two spherical particles, k and l, is as follows,

$$f_{kl}^{TOTAL} = f_{kl}^{VDV} + f_{kl}^{EDL}, \qquad (4)$$

where f_{kl}^{VDV} is the van der Waals attractive term and f_{kl}^{EDL} is the electric double layer term. These are given as,

$$f_{kl}^{VDV} = \frac{-Ar_P}{12H_{kl}^2}, \qquad (5)$$

$$f_{kl}^{EDL} = \frac{64\pi r_P n k_B T_F \Theta^2 e^{-\kappa H_{kl}}}{\kappa}. \qquad (6)$$

In the above equations, A is the Hamaker constant, r_P is the particle radius, H_{kl} is the inter-surface distance, n is the number density of electrolyte ions, k_B is Boltzmann's constant, T_F is the fluid temperature, Θ is the reduced surface potential and κ is the inverse Debye length. Particle-phase properties are presented in Table II. Note that the relative DLVO parameters favour the effect of van der Waals forces to encourage particle agglomeration, however both chemical and material properties are indicative of calcite particles in water.

3   Results & discussion

Since Rosales and Meneveau (2005) demonstrate a lack of reliance on the spectral state of the initial condition, the continuous phase for both Re_λ boxes is developed from the Arnold-Beltrami-Childress flow, a steady solution to the NS equations with a well-defined turbulent energy spectrum. The initial condition is,

$$\begin{aligned} u_F &= \cos(y) + \sin(z) \\ v_F &= \sin(x) + \cos(z) \\ w_F &= \cos(x) + \sin(y). \end{aligned} \qquad (7)$$

Figure 1 presents contour plots for both the $Re_\lambda = 29$ and $Re_\lambda = 197$ systems illustrating the velocity magnitude of the resulting turbulence field.

One consequence of linear forcing is that the relevant turbulence length scale $l = u'^3_{rms}/\epsilon$ converges on $l \sim 0.19L$, where ϵ is the viscous energy dissipation rate and $L = 2\pi$ is the domain length. Figure 2 shows the evolution of the mean of the three rms velocity fluctuation components, $\langle u'^2_{rms} \rangle$. Note that here the non-dimensional timescale $t' = t/\tau$, where $\tau = l/u'_{rms} = 4.97$ for $Re_\lambda = 29$ and $\tau = 2.05$ for $Re_\lambda = 197$.
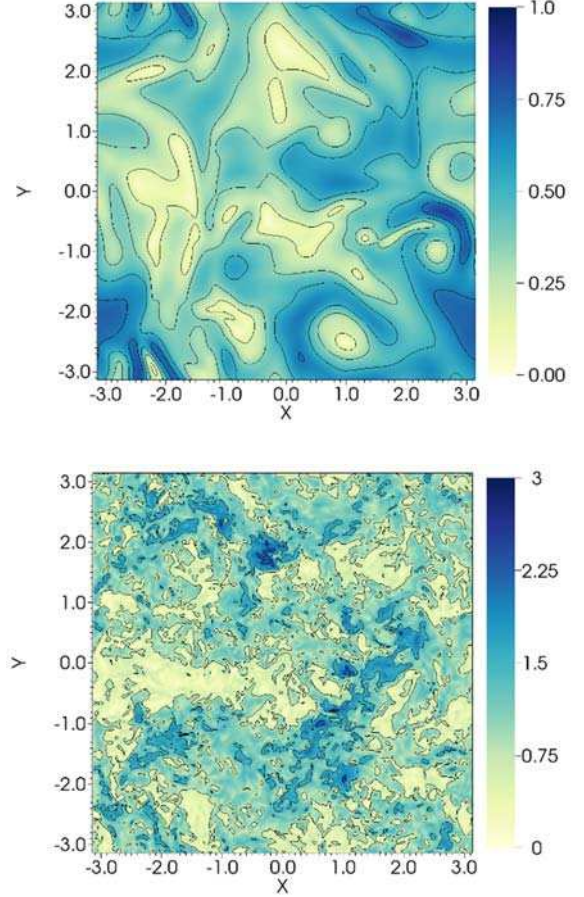

Figure 1: Contour plot of velocity magnitude (ms^{-1}) for $Re_\lambda = 29$ (upper) and $Re_\lambda = 197$ (lower) sampled from steady state (slice through $z = 0$).
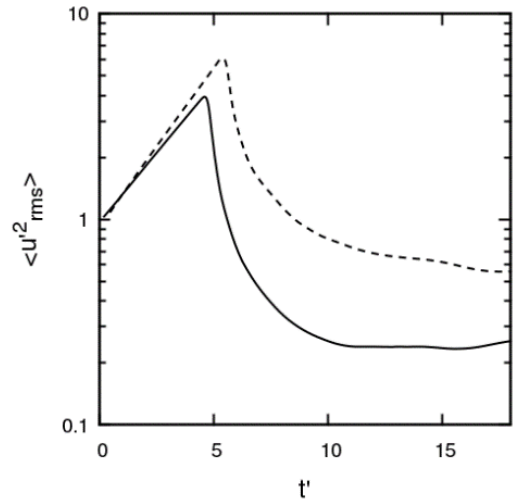

Figure 2: Contour plot of velocity magnitude (ms^{-1}) for $Re_\lambda = 29$ (upper) and $Re_\lambda = 197$ (lower) sampled from steady state (slice through $z = 0$).

In both cases, the initial transient period involves an increase in kinetic energy as the dissipation associated with the initial solution is greatly outweighed by the forcing's energy injection. At around $t' = 6$, both systems undergo a sudden transition into turbulence. The dissipation from thereon works to reduce the kinetic energy of the system until the steady state, where the forcing injection and turbulent energy dissipation are approximately equivalent. It is from time varying solutions of this final state that particle simulations are performed.

For both systems, two identical particles are injected with relative initial velocity vectors matching those most commonly occurring from collision events sampled in the equivalent region of a previously performed multi-phase channel flow simulation at $Re_\tau = 180$ (Mortimer et al., 2016). In these prior simulations, particle streamwise velocities have the mean particle streamwise velocity at their corresponding wall-normal distance subtracted from them, to account for the shift to isotropic turbulence in the present work. The results below demonstrate typical simulations within the $Re_\lambda = 29$ and $Re_\lambda = 192$ systems, but each was repeated three times to ensure consistent qualitative findings.

Figure 3 demonstrates a snapshot of the $Re_\lambda = 29$ system at $t' = 5$ (the moment of collision), with a slice through the centre of both particles illustrating velocity magnitude as in Fig. 1. A trail of increased velocities can be observed inferring the particles' trajectories through the turbulence field. These are bounded by local regions of low velocity magnitude. It is important to note that the particles are travelling in the negative x direction before this collision event takes place, hence the curving of the trails.
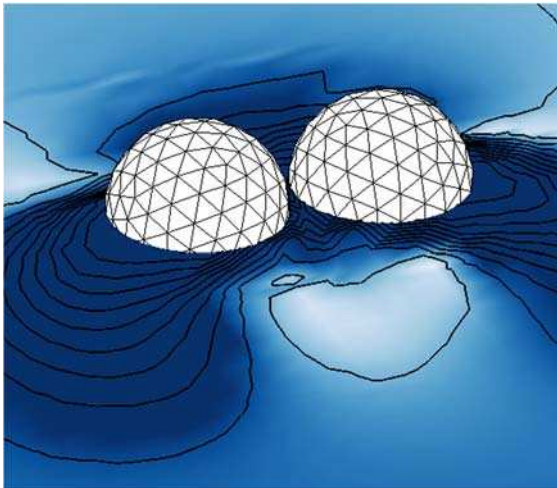

Figure 3: Contour plot of velocity magnitude for two colliding particles in $Re_\lambda = 29$ flow field at $t' = 0.05$.

Figure 4 plots the relative separation for both particles (calculated as the difference in position of particle centroids). Clearly, for the low Reynolds number turbulence field, the dominant force is van der Waals attraction which encourages the particles together. After this point they remain at constant separation, indicative of an agglomeration event. Conversely the particle pair moving in the high Reynolds number turbulence field do not collide despite moving close (within 3 particle diameters) to each other.
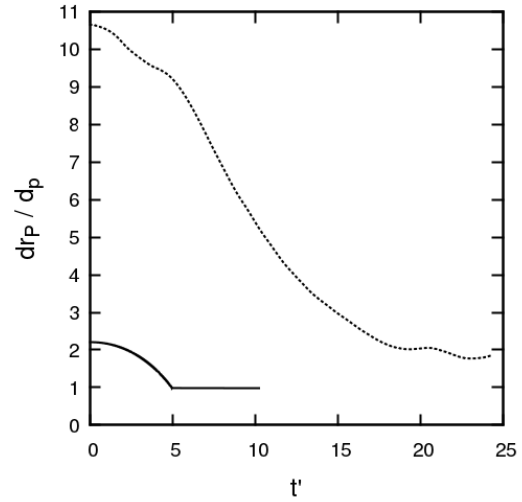

Figure 4: Time evolution of relative particle displacement normalised by particle diameter, d_P in different turbulence levels. $Re_\lambda = 192$ (solid) and $Re_\lambda = 29$ (dotted).

Figure 5 illustrates the relative velocity magnitude for both particles over the course of their interaction. Here, a positive value indicates attraction and a negative value indicates repulsion. For the low Reynolds number turbulence field, the particle undergoes acceleration towards the secondary particle before coming to an almost instantaneous halt. Close inspection shows a very short period of time during which the particle 'bounces' however the combination of strong attraction and a low coefficient of restitution ensures the relative distance remains low.

After agglomeration, the particle's relative velocity is zero indicating that they travel together. The particle in the high Reynolds number field undergoes a much more chaotic motion, showing increased response to the turbulent fluctuations it encounters. The motion and velocity of the particle in this case seems to be governed by the turbulence field rather than the attraction from van der Waals forces. In all three simulations for each turbulence level the same behaviour was observed.
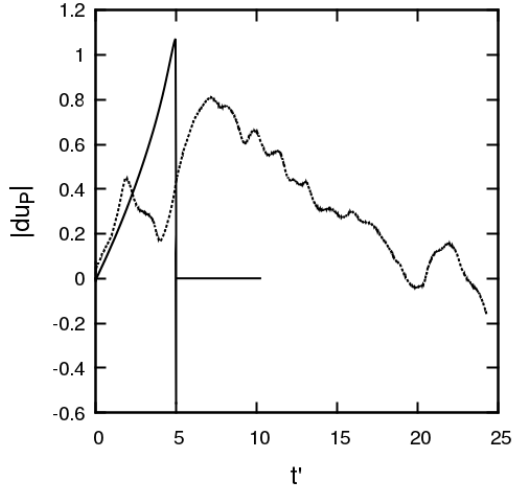
Figure 5: Time evolution of relative particle velocity magnitude in different turbulence levels. $Re_\lambda = 192$ (solid) and $Re_\lambda = 29$ (dotted).

The two results here have consequences for the analysis of turbulent channel flows in that they imply that particle-particle agglomeration events are more likely in regions of low turbulent Reynolds number, at least for the shear Stokes number of the particles simulated presently ($St^+ = 0.1$). However, previous simulation work indicates that particle agglomeration is more likely to occur in the wall-region. It is the author's opinion that this may be since collisions happen at a much greater rate in those regions, and therefore agglomeration events have an increased chance of occurring, despite having a low frequency based on a singular event.

Figure 6 illustrates the angular velocity of a particle spinning around its z axis throughout its trajectory. A positive value indicates a clockwise rotation whereas a negative value indicates a counter-clockwise rotation. For the agglomerating system at $Re_\lambda = 29$, there appears to be very little rotation occurring with very low values for angular speed throughout. An observation of interest is that at $t' = 5$, there appears to be an impact on the angular velocity as the particles collide, causing an eventual reduction in the angular velocity of one particle, and an increase in the other.

The particle in high turbulence shows much more response in terms of its rotational motion, with both particles changing direction of spin as they undergo their motion. Furthermore, their rotation speeds are much greater throughout, with a greater range. The direction of torque on the particle is changing very frequently, which indicates the particle interacting with eddies of varying rotational directions.

Table III shows the mean value for the magnitude of each force sampled over the course of each particle's trajectory. Clearly here the dominating force in the low Reynolds number box of turbulence is the

DLVO force (which is majorly van der Waals attraction given Figs. 4 and 5). At the higher Reynolds number, the effect of DLVO attraction is diminished (since the primary particle spends less time within close proximity of the secondary particle) and the hydrodynamic forces increases, becoming the primary influence on the trajectory of the particle.

Re_λ	29	197
Hydrodynamic	0.020	0.042
DLVO	0.707	0.013

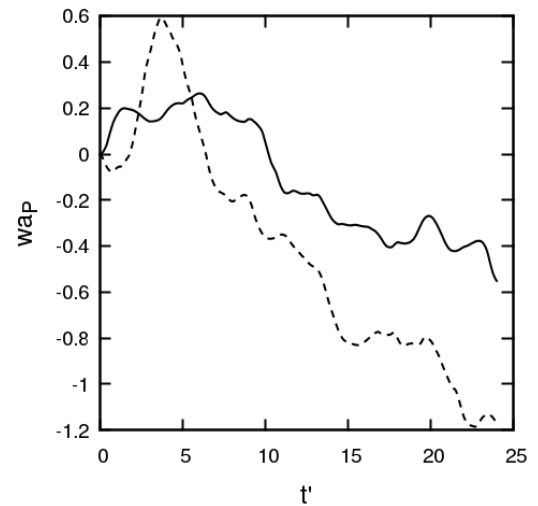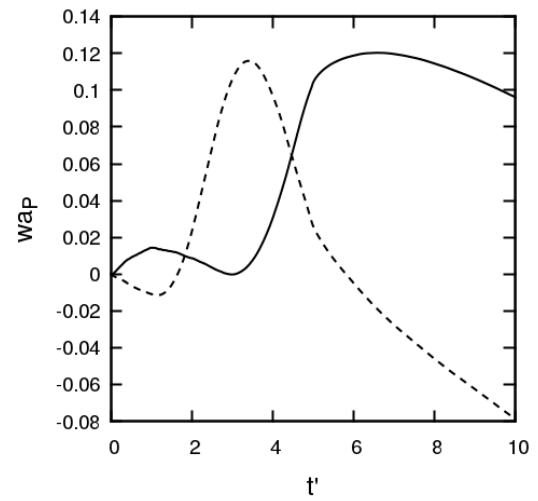TABLE III. Mean force magnitudes over course of particle trajectory.

Figure 6: Time evolution of angular velocity around its z axis for both particles at different turbulence levels. $Re_\lambda = 192$ (lower) and $Re_\lambda = 29$ (upper).

4   Conclusions

A second-order accurate immersed boundary method has been implemented in the spectral element based DNS code, Nek5000. This has been used to predict binary particle interaction events at small scales using DLVO forcing. Periodic boxes of isotropic turbulence at two different Reynolds numbers based on the Taylor microscale have been obtained using the linear forcing method.

Particle-particle interactions have been simulated in these boxes using an immersed boundary solver. The ghost-cell method is used to ensure the no-slip condition on the particle surface is met. Particles were injected with initial conditions matching those present in pre-collision events sampled from a turbulent channel flow performed with identical dispersed particles at $Re_\tau = 180$.

Slices of velocity magnitude contour plots are presented for both levels of turbulence, with each possessing their own eddy length spectra and range of velocities. The transition from initial conditions to steady state isotropic turbulence is also demonstrated, with temporal plots of the mean velocity fluctuation throughout the box.

For each system, the trajectory, velocity and angular velocity are monitored and illustrated. It is evident that agglomeration takes place in the low Reynolds number system, whereas for the high Reynolds number system, the particles are encouraged together only slightly, with turbulent fluctuations dominating the bulk of the motion. This is further confirmed by a force magnitude analysis over the course of each particle's trajectory. It is indicated that in the high Reynolds number system, DLVO forces account for around 24% of all the forces acting on the particle throughout its entire motion. This is in high contrast with the low Reynolds number system, for which the DLVO forces are entirely dominant.

The work presented in this paper provides a basis for further studies into particle-particle interactions via high fidelity simulation methods. For future work, the effect of particles Stokes number and fluid/solid material and chemical properties should be investigated to further elucidate the processes responsible for agglomeration and collision events.

References

Derjaguin, B. and Landau, L. (1941), Theory of the stability of strongly charged lyophobic sols and of the adhesion of strongly charged particles in solutions of electrolytes. *Acta physicochim.* 14, 633-662.

Fischer, P. F., Lottes, J. W. and Kerkemeier, S. G. (2008), Web page: http://nek5000.mcs.anl.gov.

Hu, H. H. (1996), Direct simulation of flows of solid-liquid mixtures. *Int. J. Multiph. Flow.* 22, 335-352.

Lundgren, T. (2003), Linearly Forces Isotropic Turbulence. Minnesota Univ Minneapolis.

Mark, A. and van Wachem, B. G. (2008), Derivation and validation of a novel implicit second-order accurate immersed boundary method. *J. Comput. Phys.* 227, 6660-6680.

Mortimer, L., Fairweather, M. and Njobuenwu, D. O. (2016), Effect of Four-Way Coupling on the Turbulence Field in Multi-Phase Channel Flows. ETMM11.

Njobuenwu, D and Fairweather, M. (2015), Dynamics of single, non-spherical ellipsoidal particles in a turbulent channel flow. *Chem. Eng. Sci.* 123, 265-282.

Peskin, C. S. (2002), The immersed boundary method. *Acta numerica.* 11, 479-517.

Rosales, C. and Meneveau, C. (2005), Linear forcing in numerical simulations of isotropic turbulence: Physical space implementations and convergence properties. *Phys. Fluids.* 17, 095106.

Short, M. P. et al. (2013), Multiphysics modeling of porous CRUD deposits in nuclear reactors. *J. Nucl. Mater.* 443 579-587.

Tseng, Y. H. and Ferziger, J. H. (2003), A ghost-cell immersed boundary method for flow in complex geometry. *J. Comput. Phys.* 192, 593-623.

Verwey, E.J.W. and Overbeek, J. T. G. (1955), Theory of the stability of lyophobic colloids. *J. Colloid Sci.* 10, 224-225